Influence of Lanthanum on Stern Layer Conductance in the Nanochannel

Manon Giraud, François-Damien Delapierre, Sokhna Mery Ngom, Isabelle Le Potier, Antoine Pallandre, Anne-Marie Haghiri-Gosnet, Jean Gamby

Influence of Lanthanum on Stern layer conductance in nanochannel

Manon Giraud,[1,†] François-Damien Delapierre,[1] Sokhna Mery Ngom,[1] Isabelle Le Potier,[1] Antoine Pallandre,[2] Anne-Marie Haghiri-Gosnet, [1] and Jean Gamby,[1,*].

(1) Université Paris-Saclay, CNRS, Centre de Nanosciences et de Nanotechnologies, 91120, Palaiseau, France. (2) Université Paris-Saclay, CNRS, Institut de Chimie Physique, UMR8000, 91405 Orsay, France.

ABSTRACT: In this report, high-frequency electric impedance spectroscopy was performed to investigate ionic transport through nanochannels. Special attention was focused on i) conductance behaviors depending on the role of cation valence in three background electrolytes (XCln): monovalent 1-1 (K^+, Cl^-), divalent 2-1 (Mg^{2+}, $2Cl^-$), and trivalent 3-1 (La^{3+}, $3Cl^-$), ii) the effects of proton and bicarbonate ions on bulk and surface conductance; and iii) the connected microchannel dimension (surface/height ratio aspect) within the nanochannel apparent conductance. The results highlight a net quantitative increase in surface silanol density and a strong decrease of surface ionization degree when Lanthanum cation is employed. The results also demonstrate that La^{3+} strongly interacts with the silica surface, leading to negative values of standard free energy for ion-site interactions and chemical potential for ion-ion correlations in the stern layer of -0.8 *k*T and -10.2 *k*T, respectively. We ascribed the evolution of surface charge density to the balance between the mole ratios of water molecules and adsorbed cations at equilibrium. We found that La^{3+} behaves as an acidic cation (Lewis conceptualization) that neutralizes the negative silica surface accompanying water molecule expulsion due to steric hindrance. This study constitutes a new contribution to ion-site interactions and to ion-ion correlations phenomena on planar silica surface to explain charge inversion observation in micro nanofluidics devices.

Introduction

The determination of surface charge density at conducting or non-conducting surfaces is a crucial element for tuning electrostatic interactions at solid/ liquid interfaces [1,2,3,4,5,6,7]. This parameter may affect membrane selectivity, electrode capacitance, particle synthesis, colloidal stability, catalysis, nucleic acid condensation, and transport through ion-channels, or micro-nanofluidic channels, among other things [8,9,10,11,12,13,14,15,16,17,18,19,20,21]. Typically, for solid-state nanofluidic devices manufactured in glass, the surface groups are ionized during the well-known acid-base deprotonation reaction, such as silanol groups, leading to a charged surface [22,23,24,25].

Due to their significance for the charge inversion (CI) phenomena, ion-ion and/or ion-site correlation effects have attracted researchers attention [26,27,28,29,30,31]. This impact was seen and reported mostly for surface-charged materials that were immersed in mono and/ or multivalent electrolytes [28,32,33,34].

In brief, the measured apparent charge appears to be of the opposite sign to that of the bare surface, meaning that the surface bears counterions in excess of (over-screening) its own nominal charge. In micro-nanofluidic devices, streaming current [35,33], open circuit potential measurements [32,36], conductance measurements [25,32] and numerical calculations [12,30,36,37] are recent approaches used to establish and define the conditions for CI observation.

Despite the large number of articles that address this topic, no consensus has been found on the exact contribution or predominance of ion-site interactions over ion-ion interactions for the origin of charge inversion [38]. For example, in the study by Dove et al [5], the role of ion-site interactions is the primordial parameter, whereas in the study by Labbez et al, [30] it is rather the major role of ion-ion interactions that is considered as preeminent. These apparent contradictions could be explained by different approaches of the same problem, i.e., an exclusively chemical approach of the interface (mainly specific chemical bonding or adsorption) and a purely physical approach of the interface (Coulombic interactions, including charge correlations) of the charge inversion (CI) phenomenon [38]. Along with this, Martin-Molina et al, [39] evidenced net charge inversion observations, especially in the context of their works about chemical interactions at soft interfaces (like liposomes), where the effects of counterions solvation and hydration by amphiphilic molecules, rather than surface charge, primarily control the inversion charge mechanism.

In this paper, we used a recently improved impedance conductance model to accurately determine the surface charge that develops at micro nanofluidic glass devices filled with asymmetric chloride electrolytes by varying the cation valence (+1, +2, and +3). We observe that models abundantly used in the literature in the case of symmetric 1:1 electrolytes do not reach a proper fit for the asymmetric electrolytes, affecting the proper determination of surface charge, local concentration of counterions in the Stern layer, and the magnitude of electrostatic forces generated [37]. The obtained data were then analysed for discrimination of bare surface charge (σ_b) in presence of cation and the extrapolated effective surface charge in Stern layer (σ_S) at equilibrium, as well as determination of standard free energy ($\Delta\mu^o$) of ion-site interactions and chemical potential of ion-ion spatial interactions (μ_c). Finally, we discussed how the lanthanum cation simultaneously influences

the degree of dissociation of a silica nanochannel to decrease and its overall surface site density to increase making the surface hydrophobic by strong dehydration at the nanochannel surface. This latter point constitutes the first and most crucial step, before ion-site interactions as complexation models suggest, and/or ion-ion interactions as strongly correlated liquid (SCL) theory suggests (SCL) [27,28]. Indeed, as for soft interfaces, here in case of solid-state interfaces, the surface charge is not the only one parameter that influences charge inversion mechanism [39].

Experimentals

Chemicals and reagents. As the micro-nano-microfluidic (MNM) device is in glass (negatively charged when in contact with water), three different cations were chosen: K^+, Mg^{2+} and La^{3+}, having Cl^- as counterions. For this goal, Potassium chloride (KCl), Magnesium chloride hexahydrate ($MgCl_2$, $6H_2O$) and Lanthanum chloride heptahydrate ($LaCl_3$, $7H_2O$) salts were purchased from Sigma-Aldrich and aqueous solutions were prepared (from 3 mol L^{-1} to 3 10^{-6} mol L^{-1}). Please note that in these experiments, unbuffered solutions were employed as a first step because we want the interactions of the cations with the surface to generate a significant shift in pH. Indeed, we believe that utilizing buffered solutions will obscure the effects we want to observe.

Since ion valence, z_i, and concentration $[i]$ are the two studied parameters, the ionic strength, I, of the solution has often been used in this work. For a solution of N ions, i, the ionic strength is defined as follows,

$$I = \frac{1}{2}\sum_{i=1}^{N}[i]z_i^2 \qquad (1)$$

Nanochannel Networks. The MNM device is presented in Figure 1, and its theoretical dimensions are given in Table 1. This latter was fabricated in borosilicate glass chip with a 1.47 ± 0.01 µm height microchannel and a 150 ± 25 nm height nanochannel. Nanochannels were made using the following process: 1) Firstly, 300 nm of amorphous silicon (α-Si) is deposited by plasma-enhanced chemical vapor deposition on a 500 µm glass wafer. 2) Then AZ-5214 reversible photoresist is spin-coated (5000 rpm, 30 s) on the glass substrate. 3) The microchannels are designed by UV lithography on a SUSS MicroTec MJB4 mask aligner. 4) In the regions that are not protected by the resin, the α-Si is etched by reactive-ion etching (RIE) with SF_6. 5) The microchannels are then etched, where α-Si does not protect the glass, using ammonium fluoride – hydrofluoric acid mixture (AF 875-125, etching mixture, Aldrich). 6-9) The nanochannel is made using the same method after a second spin-coating, lithography, and RIE (SF_6). 10) The reservoirs where solutions are injected are drilled by sandblasting. 11) The remaining α-Si is removed using RIE (SF_6). 12) The glass chip and another 300 µm glass wafer are then carefully washed using, firstly, trichloroethylene, acetone and isopropyl alcohol, secondly, for a few seconds, the etching mixture, and thirdly deionized water. 13) Finally, these two wafers are bonded without any intermediate layer using a wafer bonder SB6 (SUSS MicroTec). During thermal bonding, wafers are put in contact for 2h under vacuum at 550°C with an applied pressure of 3-5 bars. 14) A 5 mm layer of polydimethylsiloxane (PDMS) with holes aligned with the reservoirs is bonded onto the chip using air plasma (70 s). The NMN is mounted on a homemade chip holder and the electrolyte is introduced using a pressure pump controller apparatus (Elveflow).

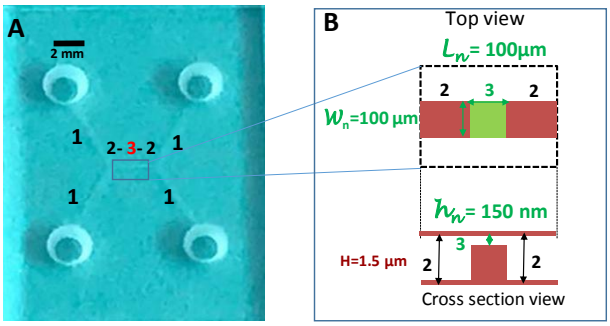

Figure 1. A. Photography of final device MNM bearing a nanochannel. At each corner, four holes (1) are used for the electrolyte injection. The microchannel (2) is reduced to a nanometric size over a short distance (see nanochannel networks) to obtain the nanochannel (3) in the center. **B**. Top and cross section views of the nanochannel with its dimensions (L_n = 100 µm; W_n = 100µm, h_n = 150 nm). See table 1.

Table 1. Dimensions of the MNM glass device described in Figure 1, where L_1, L_2, $L_{2'}$ and l are the lengths of the two external microchannels (1), the two connected microchannels (2), and the nanochannel, respectively. H_1, H_2, and h are the heights (depths) of external, connected and nanochannel, respectively. W_1, W_2 and w_n, are widths of external, connected, and nanochannel, respectively.

Channel	Length		Width	Height
External microchannel (1)	L_1		W_1	H_1
	3489 µm		352.6 µm	1.4 µm
Connected microchannel (2)	L_2	$L_{2'}$	W_2	H_2
	780 µm	785 µm	100 µm	1.5 µm
nanochannel (3)	l		w	h
	100 µm		100 µm	150 nm

Instrumentation and measurement. High-frequency electric impedance spectroscopy (HFEIS) measurements were performed using a frequency response analyser (FRA 1255B) coupled with a dielectric interface (DI 1296A) which extends the frequency range up to 20 MHz. This set-up enables measurement on high resistive systems such as nanochannels integrated into microfluidic chips. Experiments were performed with a two-electrode cell configuration. The anode and the cathode were both Ag|AgCl electrodes located in the

microchannel holes (1) as mentioned in Figure 1. Impedance changes between the two Ag|AgCl wires are measured by the paths passing through the nanochannel (3) in Figure 1. The frequency range used for HFEIS measurements was varied from 10 MHz to 1 Hz. The sinusoidal AC signal excitation between Ag|AgCl wires is set to 100 mV peak to peak, since DC was fixed to 0 V [40] .

Experimental protocols. To measure the global MNM conductance, the procedure described below was followed for various concentrations of supporting electrolyte. The MNM device was first cleaned with bi-distilled water. Then the lowest concentration $LaCl_3$ solution ($3x10^{-6}$ mol L^{-1}) was introduced into the chip through tubing controlled by a pressure pump. Once the chip was filled, the entrance pressure was set to 0. After a stabilization time of over 45 minutes, the HFEIS measurement was performed in frequencies (from 10 MHz to 1 Hz). All measurements were repeated three times. The same procedure was used for all $LaCl_3$ solutions, increasing the concentration by one order of magnitude each time up to the highest concentration of 3 mol L^{-1}. Then the channel was rinsed with bi-distilled water and kept in water overnight to ensure ion desorption. The experiments were repeated with $MgCl_2$ and, after a second cleaning protocol, with KCl.

HFEIS measurements protocol. The experimental data consist, for each concentration, of a set of three HFEIS spectra acquisitions according to the Nyquist plot representation, *i. e.*, the imaginary part of the impedance, $Z_j(\omega)$, plotted against the real part of the impedance, $Z_r(\omega)$. In brief, the semicircle (R//C time constant) observed in Figure 2A suggests that the nanochannel resistance, R (Ω), is in parallel association with C (F) which could be viewed as geometric capacity linked to concentration polarization [40]. Indeed, a shifted maximum frequency (f_{RC}) associated with the R//C time constant mentioned above is illustrated in Figure 2B. The latter can be graphically determined at the maximum value for imaginary part Z_j, which also corresponds to R/2. From those three measurements, resistance values, R, represented in Figure 2A as semi-circle diameter, are estimated according to the procedure explained in our previous paper. [40] Briefly, the asymptotic limits of the resistance at zero-frequency, R_{LF}, and those as frequency increases towards, R_{HF}, can be used to estimate the nanochannel resistance, R_{LF}-R_{HF}, on the real axis (Figure 2A). As seen on the real axis, when R_{HF} is minimal, the nanochannel resistance identifies with R_{LF}. As highlighted in Figure 2B, mentioned above, from R and the read value for the maximum f_{RC} on the Z_j plots, the capacity in parallel can be estimated at around 2.5 pF.

The obtained average values of the MNM global conductance, G (R^{-1}), related to $LaCl_3$ concentrations are listed in Table S1 (see supporting information file). The same measurement protocol was carried out with $MgCl_2$ and KCl BGE and synthetized on a *C-G* or *I-G* plot (Figure 2C-D) showing the influence of ionic concentration (C) or ionic strength (I) with conductance (G) in log-log scale representation, respectively.

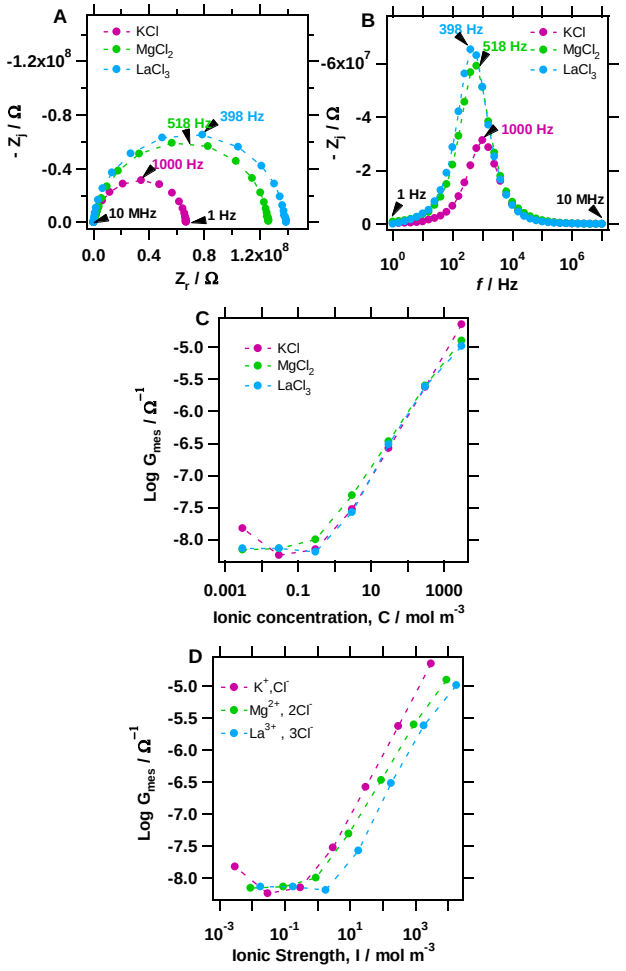

Figure 2. A. Nyquist representation of electric impedance data of a 160-nm-height nanochannel measured in a 3×10^{-6} mol L^{-1} XCl_n electrolyte solution for frequencies from 10 MHz to 1 Hz. The diameter loop allows a quick estimation (see Table S1 in supporting information) of the nanochannel resistance. B. Bode representation of the imaginary part with the applied frequency range, where the maximum frequency value, f_{RC}, reflects the observed R//C time constant. C. Measured conductances across the nanochannel against the XCl_n ionic concentration (C-G plots). D. The same data using ionic strength instead of ionic concentration with conductance (I-G plots) where a net conductance shift is observed. Here I equals to C, $3C$ and $6C$ for KCl, $MgCl_2$ and $LaCl_3$, respectively.

As expected, *I-G* plots display two main behaviors well-known in the literature, [4,41,42,40]. At low concentration, the conductance is independent of ionic strength, while at high concentration (around 1 mol m^{-3}), the conductance rises linearly with ionic strength. However, there are several first observations from the conductance plots to be mentioned: (i) The K^+ plot exhibits a re-increase of conductance at lower concentration ($3\ 10^{-3}$ mol m^{-3}) while the Mg^{2+} and La^{3+} plots do not; (ii) the conductance plateau length appears to be greater for La^{3+} than for Mg^{2+} and K^+, resulting in a concentration-shift of the linear conductance part; (iii) La^{3+} exhibits a slight decrease in conductance at the intermediary concentration (3 mol m^{-3}) whereas $Mg^{2+}$and K^+ do not, and (iv) for the highest concentration points, Mg^{2+} and La^{3+} plots deviate from the linear

tendency whereas the K^+ plot does not. Concerning this latter point, it is important to stress here that for high ionic strength, the approximation between concentrations and chemical activities (Davies and Debye-Hückel limiting law) is not valid. This tendency is critical in microfluidic structure with nanochannels since the surface charge is more influenced by the ionic strength and permits to explain why we found a deviation on the linear part of conductance. Indeed, in Figure 2, the measured conductance depends to the ionic strength since the valence of cation is a squared value in Equation 1.

Results

Nanochannel conductance characterization. The bulk and surface conductances, G_B and G_S, are superimposed to describe the two main origins of a nanochannel conductance, G_n, according to the most often used equation in the literature [41,40]. In equation (2), G_B stands for the bulk conductance of the nanochannel, which varies linearly with ionic concentration and mobilities, and G_S stands for the surface conductance of the nanochannel, which is found close to the solid surfaces of the nanochannel, as follows

$$G_n = zF(\mu_X + \mu_{Cl-})[i]h\frac{w}{l} + 2\mu_X\sigma_b\frac{w}{l} \qquad (2)$$

where μ_X and μ_{Cl-} ($m^2V^{-1}s^{-1}$) are the cation (X^{n+}) and anion (Cl^-) mobility, respectively. [i] is the ionic concentration, z is the absolute value of z_i (see Equation 1), F (C mol^{-1}), is the Faraday constant, h, w and l (m) are respectively the height, width and length of the nanochannel, σ_b (C m^{-2}) here is the bare surface charge of silica.

Given that in our chip $w = l$, as shown in Figure 1 and Table 1, the Equation (2) was reduced as follows:

$$G_n = zF(\mu_X + \mu_{Cl-})[i]h + 2\mu_X\sigma_b \qquad (3)$$

However, the preliminary fits highlighted that the widely used Equation (3) model for symmetric 1:1 electrolytes does not produce a reasonable fitting for asymmetric electrolytes. It is obvious that the nature of cation interacting with the surface conductance σ_b must be taken into consideration to improve the nanochannel conductance law in Equation (3).

Firstly, the surface charges are pH-regulated to the equilibrium between SiOH and SiO^- groups at the solid/liquid interface because the chip was designed on glass (silicate), as follows

$$SiOH + H_2O \rightleftarrows SiO^- + H_3O^+ \qquad (4)$$

$$\sigma_b = e\,\frac{\Gamma_t\,10^{-pKa}}{10^{-pKa}+10^{-pH}} \qquad \text{where } K_a = \frac{[SiO^-][H_3O^+]}{[SiOH]} \qquad (5)$$

With, e (C) being the electron charge, Γ_t (m^{-2}) is the total surface site density of SiOH groups estimated at 8 nm^{-2} [6,23,25,18].

It is important to stress that the equilibrium constants and thus the equations used to calculate the pKa in diluted solutions implies the concentrations as an approximation of the chemical activities. Finally the nanochannel conductance model relied in the following equation, as follows,

$$G_n = F\sum_i \mu_i[i]h + 2\,\mu_+ e\,\frac{\Gamma_t 10^{-pKa}}{10^{-pKa}+10^{-pH}} \qquad (6)$$

where μ_i and μ_+ ($m^2V^{-1}s^{-1}$) are the mobility of ion i, and the average mobility value of the involved cations, X^{n+} and H^+ in relation to their ionic concentrations, respectively. The approach is more sophisticated than in Equation (3) to accurately express the ionic concentrations determined by taking into consideration the addition of protons and carbonate ions in BGE solutions. The Equation (6) model now includes four ions: X^{n+} (which is La^{3+}, Mg^{2+} or K^+), Cl^-, H^+ and HCO_3^-. The mobilities and concentrations of these several species were taken into consideration in Equation (6) to determine more precisely the solution conductance.

Electroneutrality is taken into account in equation (7) below in order to add dependency between parameters during the fitting procedure for both negative and positive ions. In this instance, all of the concentrations are connected as follows,

$$[H^+] + [X^{n+}] = [HCO_3^-] + [Cl^-] \qquad (7)$$

Secondly, the acidity of BGE is caused by the carbonic acid/bicarbonate, H_2CO_3/HCO_3^- acid base equilibrium, which may be written as,

$$K_c = \frac{[H^+][HCO_3^-]}{[H_2CO_3]} \qquad (8)$$

where K_c represents the H_2CO_3/HCO_3^- acid base equilibrium equal to $1x10^{-6.37}$.

To sum up, the following expressions for the various ionic concentrations (where C, is the ionic concentration in XCl_n), are

$$[H^+] = 10^{-pH+3} \qquad (9a)$$

$$[HCO_3^-] = 10^{-8,29+pH} \qquad (9b)$$

$$[X^{n+}] = nC \qquad (9c)$$

$$[Cl^-] = nC + 10^{-pH+3} - 10^{-8,29+pH} \qquad (9d)$$

At this stage, seven parameters are subject to change: pH, pKa, h, μ (for the four ions). Equations (6) – (9) are used to make several tests. Firstly, all the parameters are kept free. Secondly, μ , and then, h are fixed. Table S2 (see supporting information) compiles all the results and illustrates how, despite the correlation coefficients (χ^2) which seem adequate for all the tests, the physical meaning of the found values can leave some doubts. Indeed, it can be noticed that even if the parameters obtained with $LaCl_3$ in table S2 seem to meet all the requirements when h is fixed, the model does not make sense for the fits with KCl and $MgCl_2$ where the h values are evaluated around 550 nm instead of 150 nm. Although the modified model in Equations (6–9) produced interesting results, there are still issues that need to be solved.

Thus, thirdly, the specific design geometry of the micro/nano fluidic device must be taken into account. The chip does, in fact, have a micro/nano interface, as shown in Figure 1 and Table 1, but in earlier computations, only nanochannel

conductance (G_n) had been taken into account. There are a number of geometric elements to take into account and compare in order to determine which components of the system can be disregarded, according to the first statement by Green et al. [43] on the impact of the connected microchannels on the apparent nanochannel conductance measured. Figure 3 provides a 2-D schematic illustration of the involved interfaces for this purpose.

Figure 3. 2-D Areas and interfaces of the MNM device shown schematically (see Figure 1). Zone 1: Global resistance in the external branches (1). Zone 2: Total resistance within the connected microchannels (2). Zone 3: The two interfacial resistances and the nanoslit domain are assimilated to an ionic filter equivalent to the overall resistance in the nanoslit (3) (from 1 to 2 and 2 to 3).

By following the consideration as mentioned by Green et al [43], all these parts can be modeled by series resistances and compared to one another using the geometrical criteria from data in table 1 above. Our chip's layout assumes that $W_2 = w$ and $H_1 = H_2 = H$. Equations provided in reference [43] are used to compute the pertinent geometrical factors. The geometric factor for the external microchannel is defined, as follows

$$\frac{L_1}{HW_1} = 2.83 \times 10^{7}\, m^{-1} \tag{10}$$

Concerning the interface (1->2) between external (1) and connected microchannel (2), the geometric factor is defined, as follows

$$\frac{\bar{f}_1}{L_1} = \frac{-1}{\pi^2 HL_1}\mathrm{Re}\left(j\sum_{k=1}^{\infty}\frac{e^{jk\pi\frac{W_1}{W_2}}}{k^2}\right) < 10^{-2}\, m^{-1} \tag{11}$$

where, $\bar{f}_1$ is a nondimensional function given in reference [43].

Concerning the connected microchannel (2), the geometric factor is defined, as follows

$$\frac{L_2}{HW_2} = 1.12 \times 10^{7}\, m^{-1} \tag{12}$$

Concerning the interface (2->3) between connected microchannel (2) and the nanochannel (3), the geometric factor is defined, as follows

$$\frac{\bar{f}_2}{L_2} = \frac{1-\ln\left(\frac{\pi h}{H}\right)}{\pi WL_2} = 8.5 \times 10^{6}\, m^{-1} \quad \text{since } h << H_2 << L_2 \tag{13}$$

where $\bar{f}_2$ is a nondimensional function given in reference [43]. Concerning the nanochannel (3), the geometric factor is defined, as follows

$$\frac{l}{hw} = 6.67 \times 10^{6}\, m^{-1} \tag{14}$$

On the basis of these criteria, it is evident that only microchannel interfacial resistance $R_{1->2}$ could be neglected, whereas external, connected and interface (2->3) resistances on the measured apparent nanochannel resistance cannot be disregarded.

In our previous work, we also proposed a methodology to quantify the geometric contribution of connected microchannels on the specific nanochannel conductance (G_n) as written in Equations (15-16) for the global conductance, (G_g), as follows [44]:

$$G_g = G_n \times K_g \tag{15}$$

where $$K_g = \frac{1}{1 + G_{nano}\cdot(R_1 + R_2 + R_{2->3})} \tag{16}$$

with R_1, R_2, and $R_{2->3}$, are the resistance for external microchannels (1), for central microchannels (2), and for the interfacial between microchannel (2) and nanochannel (3), respectively.

The nondimensionlized number *K*g is a further fitting variable that depicts how connected microchannels (1,2) and their interfacial conductances interact with G_n measurements [44].

An adaptation of Equation (6) is necessary to take into account the role of microchannels (1, 2) and nanochannel (3) leading to the experimental global conductance (G_g) measurements with a geometric factor (K_g) in order to validate this assumption, as follows

$$G_g = K_g\left(\mathrm{F}\sum_i \mu_i[i]h + 2\,\mu_+ \mathrm{e}\,\frac{\Gamma_t\, 10^{-\mathrm{pKa}}}{10^{-\mathrm{pKa}}+10^{-\mathrm{pH}}}\right) \tag{17}$$

As mentioned above, It was done initially to set the ions mobilities because the experimental La^{3+} plot appears to be simpler to match than the K^+ and Mg^{2+} plots. it seems that the La^{3+} plot is easier to fit than the K^+ and Mg^{2+} plots. First, Then, both mobilities, and then height were fixed in order to fit the two additional experimental plots. Figure 4A–C displays the modeling plots and the obtained parameters are listed in Table 2. If two geometrical parameters (h, K_g) are found, the fitting procedure in the final proposed approach could be deemed satisfactory. While values of, pH, pKa, and Γ_t are in the expected range given in Table S3 (see supporting information), and χ^2 is small, it correlates well to all three experimental curves.

As postulated above, values of *K*g listed in table 2 represent the interplay between connected microchannels on the measured apparent nanochannel conductance. The values of K_g were found to be 1.31, 2.83, and 3.72 for the KCl, $MgCl_2$, and $LaCl_3$ plots, respectively. On the basis of these observations, the predicted Duhkin number (D_u) for the nanochannel (h) and the microchannels (H_1 *and* H_2) with asymmetric electrolytes has been calculated to support this claim (see Section 4 and

Table S4 in the supporting information). As detailed in the supporting information, the estimation of D_u numbers takes into account the ion valence, its ionic concentration, and the ratio between surface and bulk conductance imposed by the channel geometry. The estimated values for D_u with ionic concentration highlight that external and connected microchannels as well as nanochannels exhibit non-negligible charge surface effects in accordance with Duhkin criteria. It can be noticed that the proportionality between D_u and Kg is the same when passing from $LaCl_3$ plot to $MgCl_2$ plot, and from $LaCl_3$ plot to KCl plot. For instance, in Table S4-B (connected microchannel), when the selected working concentration is 0.3 mol m^{-3}, D_u in the microchannel is estimated to be 0.94, 1.99, and 2.93 for $LaCl_3$, $MgCl_2$, and KCl, respectively.

Table 2. Values determined for the fitted parameters using Equation (17) for MNM devices filled with each electrolyte (see Figure 3).

Parameter	K^+,Cl^-	Mg^{2+}, $2Cl^-$	La^{3+}, $3Cl^-$
K_A	3.73 10^{-8}	1.74 10^{-8}	3.12 10^{-7}
$[H^+]$	1.60 10^{-6}	2.67 10^{-7}	5.34 10^{-5}
h (m)	1.45 10^{-7}	1.45 10^{-7}	1.45 10^{-7}
μ_X ($m^2V^{-1}s^{-1}$)	7.62 10^{-8}	1.10 10^{-7}	2.17 10^{-7}
μ_{Cl^-} ($m^2V^{-1}s^{-1}$)	7.91 10^{-8}	7.91 10^{-8}	7.91 10^{-8}
μ_{H^+} ($m^2V^{-1}s^{-1}$)	3.63 10^{-7}	3.63 10^{-7}	3.63 10^{-7}
μ_{HCO3^-} ($m^2V^{-1}s^{-1}$)	4.65 10^{-8}	4.65 10^{-8}	4.65 10^{-8}
Γ_t (m^{-2})	2.21 10^{18}	1.06 10^{18}	7.77 10^{18}
K_g	3.72	2.83	1.31
χ^2	0.028	0.025	0.014

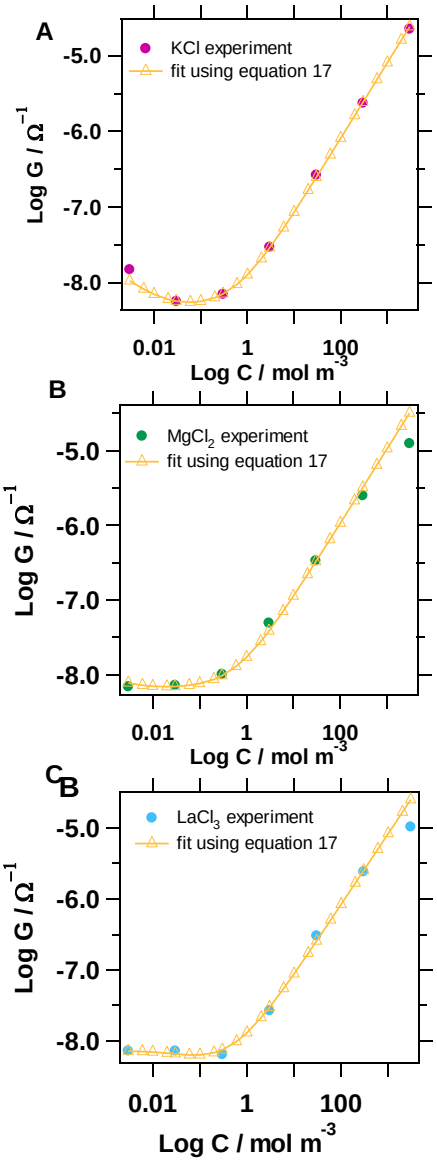

Figure 4. **A**. K^+ experimental plot fitting by using Equation (17). **B**. Mg^{2+} experimental plot fittings by the first and the second equation are quite similar. **C**. La^{3+} experimental plot fitting by the Equation (17) matches all parameters conditions (see Table 2 and Table S2 in the supporting information) and gives better results than the first and second fittings.

Discussion

Surface charge density and ion-site interaction. Here, we discuss about how to analyze the data sets that came from the plots of monovalent, divalent, and trivalent conductance. The first set of parameters seen in Table 3 demonstrates how sensitive to the cation valence the data for pH, p*K*a, Γ_t and σ_b are.

A first remark is the significant p*K*a decrease (mainly in presence of La^{3+} cation) which can be interpreted as an apparent p*K*a (p*K*a') which is shifted by modification of the silica surface. In fact, the literature generally accepts that the p*K*a value of bare silica surface is between 6 and 8 [1,22,18,45]. Here, we estimated a value of 6.87 by plotting σ_b against pKa (see table 3). In brief, this value corresponds to the extremum value of the quadratic variation $\sigma_b = f(pKa)$.

Table 3. Values determined for the fitted parameters using Equation (17) for MNM devices filled with each electrolyte (see Figure 4).

Parameter	K^+	Mg^{2+}	La^{3+}
$pKa^{\perp}$	7.45	7.76	6.50
pH	5.79	6.57	4.27
μ_x ($m^2V^{-1}s^{-1}$)	$7.62\ 10^{-8}$	$1.10\ 10^{-7}$	$2.17\ 10^{-7}$
Γ_t (m^{-2})	$2.21\ 10^{18}$	$1.06\ 10^{18}$	$7.77\ 10^{18}$
σ_b (C m^{-2})	$-8.11\ 10^{-3}$	$-10.30\ 10^{-3}$	$-7.29\ 10^{-3}$

($^{\perp}$) *pKa* value correspond to the one found by the fitting procedure in presence of each cation. This value is an apparent value named pKa' in the rest of the manuscript.

We have done the hypothesis that a strong adsorption of excess cations in the Stern layer occurs to compensate the increase in negative charges through concurrent silanol deprotonation (proton release) and adsorption of solvated cations (non-electrostatic Gibbs energy for transferring from bulk to surface). From these conditions, Equation (4) can be completed with the following equation to reflect the shift in silanol's pKa, as follows,

$$\{SiOH\cdots H_2O\} + yH_2O - X^{n+} \rightleftarrows \{SiO^-\cdots X^{n+} - yH_2O\} + H_3O^+ \quad (18)$$

$$\text{Where } K_a' = \frac{[SiO^-\cdots X^{n+} - yH_2O][H_3O^+]}{[SiOH\cdots H_2O][yH_2O - X^{n+}]} \quad (19)$$

The combination between Equations (4) and (18) leads to the following equilibrium Equation (20) that reflects the transfer of multivalent ions from the bulk solution to the Stern layer and their dehydration, as follows,

$$\{SiO^-\cdots H_2O\} + yH_2O - X^{n+} \rightleftarrows \{SiO^-\cdots X^{n+} - yH_2O\} + H_2O \quad (20)$$

We assumed that the following equilibrium constant ($K_{i\text{-}s}$) below reflects the ion-site interactions (including binding and dehydration) at silica surface, as follows

$$K_{i-s} = \frac{K_a'}{K_a} = \frac{[SiO^-\cdots X^{n+} - yH_2O]}{[SiO^-\cdots H_2O][yH_2O - X^{n+}]} \quad (21)$$

In other words, the pK_a difference (ΔpK_a) in the above Equation (21) can be viewed in terms of standard free energy [46] of the reaction ion-site interaction, $\Delta\mu°$, as follows,

$$\Delta\mu° = -kT\ ln\ K_{i-s} \quad (22)$$

where *k*T is the thermal energy expressed in [J].

The obtained values are listed in Table 4 and show a change in standard free energy, $\Delta\mu°$, related to the nature of cations involved. For instance, it was found from 1.29 *k*T to -0.836 *k*T for K^+ and La^{3+}, respectively, while it increases at 2.26 *k*T for Mg^{2+}. In accordance with previous observations in papers [28,33,36] these results evidence a strong interaction of La^{3+} with silica surface due to its first hydration shell which bears 8-9 water molecules [28] while Mg^{2+} , which bears only 5-6 molecules [47], interacts poorly with silica surface and K^+ that is considered as no having hydration shell [47].

A second remark is a net increase of the total surface site density (Γ_t) when La^{3+} is employed as BGE while the surface charge decreases according to the valence in the order Mg^{2+}> K^+> La^{3+}. Indeed, these values support that the surface charge is controlled by the prior Equation (4) as well as the previously Equations (18)-(20), which deal with proton release from surface to bulk and cation interaction in Stern layer. In order to connect the found values of $\Delta\mu°$ with the total surface site density, Γ_t, for each type of cation and their fitted parameters (pKa' and pH), another more relevant parameter can be introduced: the dissociation or ionization coefficient (α_i) of the silica interface [30,48,45], in presence of hydrated cations, can be used as follows,

$$\alpha_i = \frac{\Gamma_{SiO-}}{\Gamma_t} \quad (23)$$

where the total surface site density was previously defined as follows,

$$\Gamma_t = \Gamma_{SiOH} + \Gamma_{SiO-} \quad (24)$$

As the nanochannel interface is negatively charged, it can be assimilated as a filter or a cation retention system as in a chromatographic column [48]. The following Equation (25) can be viewed as the degree of ionization of a silica nanochannel with the acidity of silanols (Stern layer: p*K*) and the acidity of the bulk solution (mobile phase: pH), as follows,

$$\alpha_i = \frac{K_a'}{K_a' + [H^+]} = \frac{1}{1 + 10^{pKa' - pH}} = \frac{\Gamma_{SiO-}}{\Gamma_t} \quad (25)$$

This indicates that just a small portion of the entire surface area of the silanol group (Γ_t) is ionized into SiO^- form. As a result, Table 4 lists the precise values of Γ_{SiO-} (SiO^- forms) following a new evaluation. We note that whereas the total number of surface site density (Γ_t) was in the order La^{3+}, K^+, Mg^{2+}, the degree of ionization was in the order Mg^{2+}, K^+, and La^{3+}. These findings support the earlier idea that trivalent cation insertion in the stern layer enhances negative charge compensation through strong ion-site interactions that exhibit the lowest α_i value.

Table 4. Values determined for the fitted parameters using Equations (16)-(22) for MNM devices filled with each electrolyte.

Parameter	K^+	Mg^{2+}	La^{3+}
$K_{i\text{-}s}$	2.77 10^{-1}	1.29 10^{-1}	2.31
$\Delta\mu^{\circ}$ (kT) *	1.29	2.05	-0.84
α_i	2.29 10^{-2}	6.06 10^{-2}	5.85 10^{-3}
$\alpha_i \Gamma_t$ (m^{-2})	5.06 10^{+16}	6.43 10^{+16}	4.56 10^{+16}
σ_b (C m^{-2})	-8.11 10^{-3}	-10.30 10^{-3}	-7.29 10^{-3}

(*) kT stands for the thermal energy unit that results from multiplying the Boltzmann constant by the absolute temperature (here T = 293.16 K) which results in a value of 4.047 10^{-21} J.

At this point of the discussion, it should be noted that the observed decrease in surface charge σ_b (see Table 4) in presence of La^{3+} depends strongly on the standard free energy of the ion-site interaction reaction, $\Delta\mu°$, which is primarily affected by the hydrated cation's acidity and the degree of ionization of the silica surface. For each cation in contact with the silica surface, the change of σ_b can be plotted with the following parameters (Table 4), to increase confidence, as follows,

$$\sigma_b = f(\Delta\mu°) \qquad (26)$$

The plot in Figure 5 evidenced a clear observation of the exponential law in Equation (27) as shown in the linear fitting, as follows,

$$\sigma_b = -6.91 \cdot 10^{-3} - 18 \cdot 10^{-5} e^{-\Delta\mu_0/kT} \qquad (27)$$

The offset value (-6.91 mC m^{-2}) corresponds to the bare surface charge for water-silicate in the absence of a specific cation adsorption, and the pre-exponential factor value represents the amplitude change in number density of z_i cation in the stern layer.

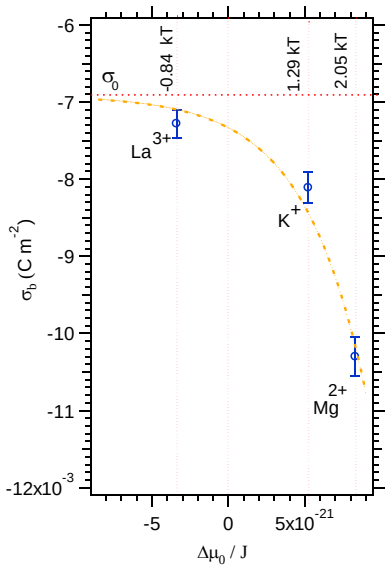

Figure 5. Exponential variation of the obtained bare surface charge plotted against the standard free energy ($\Delta\mu^0$) calculated with Equation (22). The values are summarized in Table 4.

Surface charge density and surface dehydration. By considering the balance Equation (20) where La^{3+} behaves acidic cation that neutralizes the negative silica surface accompanying with water molecule expulsion due to steric hindrance, the evolution of surface charge density can be estimated for all acidic cations in the stern layer (see Table S5 in the supporting information for molar ratio determination from Equation (20).

The equilibrium constant for t=t_{eq} in Table S5 is now written in terms of the surface site density taking into account the ionization degree (α_i), and the molar ratio (β_j) as :

$$K_{i.s}^{\Gamma} = \frac{(\beta_j \Gamma_{H2O})^2}{(\alpha_i \Gamma_t - \beta_j \Gamma_{H2O})(\Gamma_{X^{n+}} - \beta_j \Gamma_{H2O})} \qquad (28)$$

The equation (23) can be presented as a quadratic function and has the form as follows:

$$[K_{i.s}^{\Gamma} - 1](\beta_j \Gamma_{H2O})^2 + [-K_{i.s}^{\Gamma} \alpha_i \Gamma_t - K_{i.s}^{\Gamma} \Gamma_{X^{n+}}]\beta_j \Gamma_{H2O} + K_{i.s}^{\Gamma} \alpha_i \Gamma_t \Gamma_{X^{n+}} = 0 \qquad (29)$$

The derivative of the parabola function leads to a steady state permitting us to determine the water molar fraction at the equilibrium, as follows,

$$\beta_{j,eq} \Gamma_{H2O} = \frac{K_{i.s}^{\Gamma}[\alpha_i \Gamma_t + \Gamma_{X^{n+}}]}{2(K_{i.s}^{\Gamma} - 1)} \qquad (30)$$

By assuming that an homogeneous 2-*D* distribution of water monolayer at t=t_0 on the silica surface, the theoretical density of water molecules in [m^{-2}] can be estimated using its molar volume, as follows,

$$\Gamma_{H2O} = \left(\frac{N_A}{V_m}\right)^{2/3} \qquad (31)$$

with N_A is the Avogrado's number [mol^{-1}], and V_m represents water molar volume [m^3 mol^{-1}].

The Equation (31) can be also used for a theoretical estimation of the occupied density of each cation, Γ_X^{n+}, and $\beta_{j,eq}$ (see Table S5 in the supporting information) that corresponds to the molar ratio (in excess) in the Stern layer at equilibrium. The obtained values are listed in Table S6 (see the supporting information).

The evolution effective surface charge, σ_S, can be expressed from the balance Equation (20), as follows

$$\sigma_S = z_i e(\alpha_i \Gamma_t - \beta_j \Gamma_{H2O}) \quad (32)$$

with z_i=-1,

$$\sigma_S = -e\alpha_i \Gamma_t + e\beta_j \Gamma_{H2O} \quad (33)$$

At the equilibrium, the effective surface charge can be expressed as follows,

$$\sigma_{S,eq} = \sigma_{b,eq} + e\beta_{j,eq}\Gamma_{H2O} \quad (34)$$

The expression can be used to calculate, $\sigma_{S,eq}$, for each cation. The obtained values are plotted in Figure 6 A.

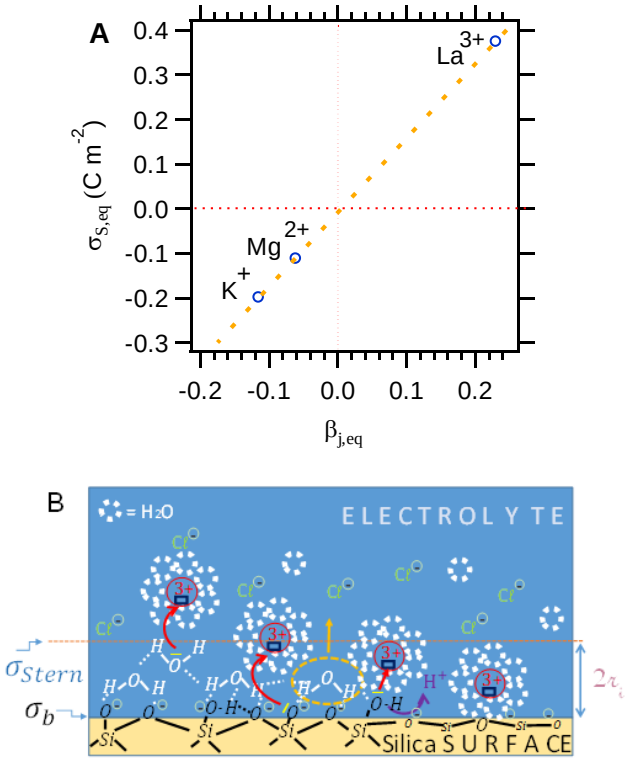

Figure 6. **A**. Plot of calculated effective surface charge in Stern layer with the molar ratio at equilibrium of water consecutive to cation adsorption in Stern layer. The equilibrium values ($\beta_{j,eq}$) are listed in S6 and calculated from Equations (30) – (31). **B**. Schematic representation of a silica-water surface (2-D layer water molecules adsorbed on it) where lanthanum cation behaves as a Lewis acid reacting both with oxygen of water and silanol leading to surface dehydration and binding, respectively. The mechanism involves proton concentration increase (see Equation (18)) and water molecules expulsion due to steric hindrance (see Equations (20)).

The plot in Figure 6 A evidenced a clear observation of $\sigma_{S,eq}$ dependence with the nature of cation and its sign inversion due to La^{3+} insertion in Stern layer.

$$\sigma_{S,eq} = -0.00895 + 1.664\,\beta_{j,eq} \quad (35)$$

The intercept corresponds to the effective bare surface charge (-8.95 mC m^{-2}), and the slope value (1.664 C m^{-2}) represents excess term related to the modification in surface charge due to water desorption in the Stern layer provoked by a cation adsorption.

The literature does not usually include this observed trend of increasing cation valence with reducing surface charge. One cause stems primarily from the difficulty to accurately determine effective surface charge and/or bare surface charge density. Additionally, it is challenging to characterize the initial glass surface state and how it changes as a result of various steps in the surface conditioning protocol (whether or not the surface is hydrated) [49]. These factors may have a significant impact on how surface charge variation in nanochannel is interpreted with silica hydrophobicity [50] and what inferences may be ascribed to it.

Surface charge density and ion-ion correlations effects. As illustrated in Figure 6 B, we are able to distinguish the precise value of the bare surface charge from the effective one induced by the cation. Now, the next step is an estimation of the chemical potential (μ_c) which takes into account the spatial interactions between Lanthanum cations in the Stern layer (La^{3+} excess in Figure 6 B) as proposed in the theory of the formation of a 2-*D* strongly correlated liquid (SCL) [27,28], as follows,

$$\mu_c = -kT(1.65\Omega - 2.61\Omega^{0.25} + 0.26ln\Omega + 1.95) \quad (36)$$

where the interaction parameter, Ω, is provided by the following expression,

$$\Omega = \frac{\left((|\sigma_b z_i^3|e^3)/\pi\right)^{0.5}}{4kT\varepsilon_0\varepsilon} \quad (37)$$

with $\varepsilon_0\varepsilon$, being the electrical permittivity equal to 8.85 10^{-12} F m^{-1}.

In order to satisfy a SCL formation that is currently reported for z_i valence levels equal to or more than 3, the Ω estimated values in this SCL model are expected to be greater than 1.

Therefore, just the first term in Equation 36 can be taken into account. According to Table 5, which summarizes the results, the Ω calculated values for the three cations range from 1.19 to 6.20, accounting for the effective bare surface charge of -8.95 mC m^{-2}. Equation 35 is then used to compute the values of μ_c, which are found at several *k*T magnitudes (see Table 5). We obtained values for K^+ and Mg^{2+} that were around -1.97 *k*T and -5.57 *k*T, respectively, while La^{3+} had a strong value of -10.20 *k*T that was in agreement with previous reports [28].

According to what is commonly believed, significant ion-ion interactions phenomena mainly appear for cations with valences of at least z_i=3 [28,36] rarely for those with z_i=2 [32], and very rarely for those with z_i=1 [34]. Because it is close to the unit, it is presumed that the need for using Equation 36 does not apply in this case. These findings may help to explain why, while this is not the case for K^+, the conductance plots for Mg^{2+} and La^{3+} cations appear to slow down (deviate from linearity) at very high concentrations due to an increase in specific correlation in the Stern layer (see Figure 2). In order to achieve this, we now calculate the theoretical electrolyte concentration that initiates the charge inversion (C_{inv}) phenomenon using the following equation [27,28,32]:

$$C_{inv} = \frac{|\sigma_b|}{2 r_i z_i e} \exp\left(\frac{\Delta\mu_0 + \mu_c}{kT}\right) \qquad (38)$$

where r_i represents the hydrated cation radius in the Stern layer (See Figure 6 B).

As indicated previously for K^+, C_{inv} in Table 5 could be disregarded because it has little physical significance due to the Ω correlation parameter being close to unit in our configuration. Furthermore, there is no effect around this C_{inv} number when considering the K^+ conductance plot with concentration. But for a rise in the valence passing from 2 and 3, there is a net drop of two orders of magnitude in the theoretical range of charge inversion concentration. Indeed, for Mg^{2+} and La^{3+}, the theoretical values approach 0.255 and 0.00139 mol m^{-3}, respectively.

Table 5. Values determined for the parameters using Equations (36)-(38) for MNM devices filled with each electrolyte.

Parameter	K^+	Mg^{2+}	La^{3+}
Ω	1.19	3.38	6.20
μ_c (kT)	-1.97	-5.57	-10.20
$(\Delta\mu^o + \mu_c)$ (kT)	-0.68	-3.57	-11.04
r_i (Å)$^{\varnothing}$	1.38	3.46	3.98
C_{inv} (mol m^{-3})	4.63 10^{1}	2.55 10^{-1}	1.39 10^{-3}

$^{\varnothing}$The indicated cation radius corresponds to the hydrated cations given in the literature [28,32,47].

These results allow us to explain why the experimental conductance plots according to ionic concentration range changed in the following ways: (i) the La^{3+} conductance plateau length was found to be longer than that of Mg^{2+} and K^+ leading to a concentration-shift on the start of linear conductance part, (ii) La^{3+} conductance plot is the only one showing a slight decrease in conductance at the intermediary concentration (3 10^{-3} - 3 10^{-1} mol m^{-3}) while it is not visible for $Mg^{2+}$and K^+, nor (iii) for the higher concentration points (3 10^{+3} mol m^{-3}), Mg^{2+} and La^{3+} plots deviate from the linear tendency unlike the K^+ plot.

It implies that the origins of the CI effects are not the same depending on the type of cation. Screening seems more critical for Mg^{2+} and K^+ and less important in the case of La^{3+}, where binding and surface dehydration occur in the Stern layer. This particularity for La^{3+} cation points to a non-electrostatic mechanism that Molina et al [39] previously demonstrated with MD simulations. Therefore, the intermediary concentration range where we observed a non-monotonic change of the measured conductance plateau matches well with the theoretical prediction of the concentration where charge inversion starts.

Conclusion

In conclusion, a methodological approach that tests the accuracy of conductance models in the literature in a variety of asymmetric chloride electrolytes (K^+, Mg^{2+}, and La^{3+}) enables the determination of the bare silica surface charge (σ_b) with greater accuracy when the effective surface charge in Stern layer (σ_S) changes with the involved cation. The more accurate simulation of nanochannel conductance accounts for the change in pKa silanols acidity in the Stern layer brought on by ion-site interactions (binding and dehydration), which is controlled by proton release from the surface to the bulk. The latter pKa shift was measured in terms of standard free energy, showing that acidic cation La^{3+} interacts strongly with the water-silica interface in contrast to K^+ and Mg^{2+}, where interactions in the Stern layer appear to be minimal. This observation was supported by measurements of variation of the surface silanol density, the estimation of water surface density, and the level of ionization degree on silica surface (hydrophobicity). The analytical model of 2-*D* creation of strongly correlated liquid of cations at silica surface was then used to estimate the theoretical concentration of charge inversion caused by ion-ion correlations. Finally, we came to the conclusion that charge inversion is initiated in first by catalytic surface dehydration through ion-site interactions on silica dominated by cation acidity, as is the case of Lanthanum (Lewis acid) with strong interaction with the negative charge of Silanol (Lewis base), and then, in second by ion-ion interaction, as measured by the huge *k*T magnitude determined specifically La^{3+} cations (accumulation in Stern layer). It was clearer from these observations that ion-site interactions are primarily detectable at intermediate concentration ranges where screening is negligible (conductance plateau) and that ion-ion correlations primarily affect intermediate to high concentration ranges through deviation from linear conductance response.

ASSOCIATED CONTENT

Supporting Information

The Supporting Information is available free of charge on the ACS Publications website.

Average values determination of MNM global conductance when Lanthanum cation is used, evaluation of the fitting procedure quality with equation (6)-(9), list of theoretical values and confidence intervals for the used parameters (pH, μ_i, pKA, h, Γ_{SiOH}), Duhkin number estimation and geometric factor K_g interpretation, estimation of theoretical molar ratios, molar volume and theoretical surface site density of each species (PDF).

AUTHOR INFORMATION

Corresponding Author

Jean Gamby – Team Smart Biosystems, MicroNanoBioFluidics department, UMR 9001 - Centre de Nanosciences et de Nanotechnologies (C2N), CNRS, Université Paris-Saclay, Université Paris Cité, 10 boulevard Thomas Gobert, 91120 Palaiseau, France ;
orcid.org/0000-0001-7613-8872
Email: jean.gamby@c2n.upsaclay.fr

Authors

Manon Giraud[†] – Team Smart Biosystems, MicroNanoBioFluidics department, UMR 9001 - Centre de Nanosciences et de Nanotechnologies (C2N), CNRS, Université Paris-Saclay, Université Paris Cité, France.

Present Addresses

[†] Epilab, 4 rue Anatole France, 78350, Jouy-en-Josas, France

François-Damien Delapierre – Team Smart Biosystems, MicroNanoBioFluidics department, UMR 9001 - Centre de Nanosciences et de Nanotechnologies (C2N), CNRS, Université Paris-Saclay, Université Paris Cité, France.

Sokna Mery Ngom – Team Smart Biosystems, MicroNanoBioFluidics department, UMR 9001 - Centre de Nanosciences et de Nanotechnologies (C2N), CNRS, Université Paris-Saclay, Université Paris Cité, France.

Isabelle Le Potier – Team Smart Biosystems, MicroNanoBioFluidics department, UMR 9001 - Centre de Nanosciences et de Nanotechnologies (C2N), CNRS, Université Paris-Saclay, Université Paris Cité, France.

Antoine Pallandre – Université Paris-Saclay, CNRS, Institut de Chimie Physique, UMR8000, 91405 Orsay, France.

Anne-Marie Haghiri-Gosnet – Team Smart Biosystems, MicroNanoBioFluidics department, UMR 9001 - Centre de Nanosciences et de Nanotechnologies (C2N), CNRS, Université Paris-Saclay, Université Paris Cité, France.

ACKNOWLEDGMENT

This work was supported by the C2N-CNRS technological platform, a member of the RENATECH network.

REFERENCES

1. Hiemstra, T.; Van Riemsdijk, W. H.; Bolt, G. H., Multisite proton adsorption modeling at the solid/solution interface of (hydr)oxides: A new approach: I. Model description and evaluation of intrinsic reaction constants. *Journal of Colloid and Interface Science* **1989,** *133* (1), 91-104.

2. Behrens, S. H.; Grier, D. G., The charge of glass and silica surfaces. *The Journal of Chemical Physics* **2001,** *115* (14), 6716-6721.

3. Lyklema, J., Specificity in the statics and dynamics of surface-confined ions. *Molecular Physics* **2002,** *100* (19), 3177-3185.

4. Stein, D.; Kruithof, M.; Dekker, C., Surface-Charge-Governed Ion Transport in Nanofluidic Channels. *Phys. Rev. Lett.* **2004,** *93* (3), 035901/1-035901/4.

5. Dove, P. M.; Craven, C. M., Surface charge density on silica in alkali and alkaline earth chloride electrolyte solutions. *Geochimica et Cosmochimica Acta* **2005,** *69* (21), 4963-4970.

6. Jiang, Z.; Stein, D., Electrofluidic Gating of a Chemically Reactive Surface. *Langmuir* **2010,** *26* (11), 8161-8173.

7. Ma, Q.; Li, Y.; Wang, R.; Xu, H.; Du, Q.; Gao, P.; Xia, F., Towards explicit regulating-ion-transport: nanochannels with only function-elements at outer-surface. *Nature Communications* **2021,** *12* (1), 1573.

8. Gurnev, P. A.; Bezrukov, S. M., Inversion of Membrane Surface Charge by Trivalent Cations Probed with a Cation-Selective Channel. *Langmuir* **2012,** *28* (45), 15824-15830.

9. Tagliazucchi, M.; Szleifer, I., How Does Confinement Change Ligand–Receptor Binding Equilibrium? Protein Binding in Nanopores and Nanochannels. *Journal of the American Chemical Society* **2015,** *137* (39), 12539-12551.

10. Gao, X.; Omosebi, A.; Holubowitch, N.; Landon, J.; Liu, K., Capacitive Deionization Using Alternating Polarization: Effect of Surface Charge on Salt Removal. *Electrochimica Acta* **2017,** *233*, 249-255.

11. Zhu, Z.; Wang, D.; Tian, Y.; Jiang, L., Ion/Molecule Transportation in Nanopores and Nanochannels: From Critical Principles to Diverse Functions. *Journal of the American Chemical Society* **2019,** *141* (22), 8658-8669.

12. Lin, K.; Lin, C.-Y.; Polster, J. W.; Chen, Y.; Siwy, Z. S., Charge Inversion and Calcium Gating in Mixtures of Ions in Nanopores. *Journal of the American Chemical Society* **2020,** *142* (6), 2925-2934.

13. Mejri, A.; Mazouzi, K.; Herlem, G.; Picaud, F.; Hennequin, T.; Palmeri, J.; Manghi, M., Molecular dynamics investigations of ionic conductance at the nanoscale: Role of the water model and geometric parameters. *Journal of Molecular Liquids* **2022,** *351*, 118575.

14. Liu, X.; Zong, X.; Xue, S.; He, M., Regulating structure and flow of ionic liquid confined in nanochannel using water and electric field. *Journal of Molecular Liquids* **2022,** *351*, 118612.

15. Grosberg, A. Y.; Nguyen, T. T.; Shklovskii, B. I., Colloquium: The physics of charge inversion in chemical and biological systems. *Reviews of Modern Physics* **2002,** *74* (2), 329-345.

16. White, H. S.; Bund, A., Ion Current Rectification at Nanopores in Glass Membranes. *Langmuir* **2008,** *24* (5), 2212-2218.

17. Besteman, K.; Van Eijk, K.; Lemay, S. G., Charge inversion accompanies DNA condensation by multivalent ions. *Nature Physics* **2007,** *3* (9), 641-644.

18. Ma, Y.; Xue, S.; Hsu, S.-C.; Yeh, L.-H.; Qian, S.; Tan, H., Programmable ionic conductance in a pH-regulated gated nanochannel. *Physical Chemistry Chemical Physics* **2014,** *16* (37), 20138-20146.

19. Forse, A. C.; Merlet, C.; Griffin, J. M.; Grey, C. P., New Perspectives on the Charging Mechanisms of Supercapacitors. *Journal of the American Chemical Society* **2016,** *138* (18), 5731-5744.

20. Ramirez, P.; Manzanares, J. A.; Cervera, J.; Gomez, V.; Ali, M.; Nasir, S.; Ensinger, W.; Mafe, S., Surface charge regulation of functionalized conical nanopore conductance by divalent cations and anions. *Electrochimica Acta* **2019,** *325*, 134914.

21. Chen, L.; Tu, B.; Lu, X.; Li, F.; Jiang, L.; Antonietti, M.; Xiao, K., Unidirectional ion transport in nanoporous carbon membranes with a hierarchical pore architecture. *Nature Communications* **2021,** *12* (1), 4650.

22. Ong, S.; Zhao, X.; Eisenthal, K. B., Polarization of water molecules at a charged interface: second harmonic studies of the silica/water interface. *Chemical Physics Letters* **1992,** *191* (3), 327-335.

23. van der Heyden, F. H. J.; Stein, D.; Dekker, C., Streaming Currents in a Single Nanofluidic Channel. *Physical Review Letters* **2005,** *95* (11), 116104.

24. Hughes, C.; Yeh, L.-H.; Qian, S., Field Effect Modulation of Surface Charge Property and Electroosmotic Flow in a Nanochannel: Stern Layer Effect. *The Journal of Physical Chemistry C* **2013,** *117* (18), 9322-9331.

25. Fuest, M.; Rangharajan, K. K.; Boone, C.; Conlisk, A. T.; Prakash, S., Cation Dependent Surface Charge Regulation in Gated Nanofluidic Devices. *Analytical Chemistry* **2017,** *89* (3), 1593-1601.

26. James, R. O.; Healy, T. W., Adsorption of hydrolyzable metal ions at the oxide—water interface. II. Charge reversal of SiO2 and TiO2 colloids by adsorbed Co(II), La(III), and Th(IV) as model systems. *Journal of Colloid and Interface Science* **1972,** *40* (1), 53-64.

27. Shklovskii, B. I., Screening of a macroion by multivalent ions: Correlation-induced inversion of charge. *Physical Review E* **1999,** *60* (5), 5802-5811.

28. Besteman, K.; Zevenbergen, M. A. G.; Lemay, S. G., Charge inversion by multivalent ions: Dependence on dielectric constant and surface-charge density. *Physical Review E* **2005,** *72* (6), 061501.

29. Faraudo, J.; Travesset, A., The Many Origins of Charge Inversion in Electrolyte Solutions: Effects of Discrete Interfacial Charges. *The Journal of Physical Chemistry C* **2007,** *111* (2), 987-994.

30. Labbez, C.; Jönsson, B.; Skarba, M.; Borkovec, M., Ion−Ion Correlation and Charge Reversal at Titrating Solid Interfaces. *Langmuir* **2009,** *25* (13), 7209-7213.

31. He, Y.; Gillespie, D.; Boda, D.; Vlassiouk, I.; Eisenberg, R. S.; Siwy, Z. S., Tuning Transport Properties of Nanofluidic Devices with Local Charge Inversion. *Journal of the American Chemical Society* **2009,** *131* (14), 5194-5202.

32. Li, S. X.; Guan, W.; Weiner, B.; Reed, M. A., Direct Observation of Charge Inversion in Divalent Nanofluidic Devices. *Nano Lett.* **2015,** *15* (8), 5046-5051.

33. Morikawa, K.; Tsukahara, T., Shift of charge inversion point of a trivalent ion solution in a nanofluidic channel. *Colloid and Interface Science Communications* **2022,** *50*, 100646.

34. Calero, C.; Faraudo, J.; Bastos-González, D., Interaction of Monovalent Ions with Hydrophobic and Hydrophilic Colloids: Charge Inversion and Ionic Specificity. *Journal of the American Chemical Society* **2011,** *133* (38), 15025-15035.

35. van der Heyden, F. H. J.; Stein, D.; Besteman, K.; Lemay, S. G.; Dekker, C., Charge Inversion at High Ionic Strength Studied by Streaming Currents. *Physical Review Letters* **2006,** *96* (22), 224502.

36. Chou, K.-H.; McCallum, C.; Gillespie, D.; Pennathur, S., An Experimental Approach to Systematically Probe Charge Inversion in Nanofluidic Channels. *Nano Letters* **2018,** *18* (2), 1191-1195.

37. Taboada-Serrano, P.; Yiacoumi, S.; Tsouris, C., Behavior of mixtures of symmetric and asymmetric electrolytes near discretely charged planar surfaces: A Monte Carlo study. *The Journal of Chemical Physics* **2005,** *123* (5), 054703.

38. Lyklema, J., Overcharging, charge reversal: Chemistry or physics? *Colloids and Surfaces A: Physicochemical and Engineering Aspects* **2006,** *291* (1), 3-12.

39. Martín-Molina, A.; Rodríguez-Beas, C.; Faraudo, J., Charge Reversal in Anionic Liposomes: Experimental Demonstration and Molecular Origin. *Physical Review Letters* **2010,** *104* (16), 168103.

40. Gamby, J.; Delapierre, F.-D.; Pallandre, A.; Tribollet, B.; Deslouis, C.; Haghiri-Gosnet, A.-M., Dielectric properties of a single nanochannel investigated by high-frequency impedance spectroscopy. *Electrochem. commun.* **2016,** *66*, 5--9.

41. Schoch, R. B.; Lintel, H. v.; Renaud, P., Effect of the surface charge on ion transport through nanoslits. *Physics of Fluids* **2005,** *17* (10), 100604.

42. Martins, D. C.; Chu, V.; Conde, J. P., The effect of the surface functionalization and the electrolyte concentration on the electrical conductance of silica nanochannels. *Biomicrofluidics* **2013,** *7* (3), 034111.

43. Green, Y.; Eshel, R.; Park, S.; Yossifon, G., Interplay between Nanochannel and Microchannel Resistances. *Nano Letters* **2016,** *16* (4), 2744-2748.

44. Ngom, S. M.; Potier, I. L.; Haghiri-Gosnet, A.-M.; Gamby, J., Modeling the role played by nanoslit lengths on conductance changes into micro nano microfluidics devices. *Electrochimica Acta* **2021,** *374*, 137930.

45. Barr, S. A.; Panagiotopoulos, A. Z., Interactions Between Charged Surfaces with Ionizable Sites. *Langmuir* **2011,** *27* (14), 8761-8766.

46. Andrieux, C. P.; Gamby, J.; Hapiot, P.; Saveant, J.-M., Evidence for Inverted Region Behavior in Proton Transfer to Carbanions. *J. Am. Chem. Soc.* **2003,** *125* (33), 10119-10124.

47. Darmois, E., Qu'est-ce qu'un ion electrolytique? *J. Phys. Radium* **1941,** *2* (1), 2-11.

48. Méndez, A.; Bosch, E.; Rosés, M.; Neue, U. D., Comparison of the acidity of residual silanol groups in several liquid chromatography columns. *Journal of Chromatography A* **2003,** *986* (1), 33-44.

49. Schrader, A. M.; Monroe, J. I.; Sheil, R.; Dobbs, H. A.; Keller, T. J.; Li, Y.; Jain, S.; Shell, M. S.; Israelachvili, J. N.; Han, S., Surface chemical heterogeneity modulates silica surface hydration. *Proceedings of the National Academy of Sciences* **2018,** *115* (12), 2890-2895.

50. Moon, H.; Collanton, R. P.; Monroe, J. I.; Casey, T. M.; Shell, M. S.; Han, S.; Scott, S. L., Evidence for Entropically Controlled Interfacial Hydration in Mesoporous Organosilicas. *Journal of the American Chemical Society* **2022,** *144* (4), 1766-1777.